

1 **Variation in the Pedersen Conductance near Jupiter's**
2 **Main Emission Aurora: Comparison of Hubble Space**
3 **Telescope and Galileo Measurements**

4 **M. J. Rutala^{1,2}, J. T. Clarke², M. F. Vogt², and J. D. Nichols³**

5 ¹School of Cosmic Physics, DIAS Dunsink Observatory, Dublin Institute for Advanced Studies, Dublin 15,
6 Ireland

7 ²Center for Space Physics, Boston University, Boston MA

8 ²Department of Physics and Astronomy, University of Leicester, Leicester UK

9 **Key Points:**

- 10
- 11 • The effective ionospheric Pedersen conductance in Jupiter's main emission auro-
12 ral region is derived from remote and in-situ measurements.
 - 13 • Field-aligned auroral currents of ~ 10 MA rad⁻¹ and effective Pedersen conduc-
14 tances of ~ 0.14 mho are derived, consistent with past research.
 - 15 • The effective Pedersen conductance varies primarily in magnetic local time, and
may explain the enigmatic motions of some auroral forms.

Corresponding author: M. J. Rutala, mrutala@bu.edu

Abstract

We present the first large-scale statistical survey of the Jovian main emission (ME) to map auroral properties from their ionospheric locations out into the equatorial plane of the magnetosphere, where they are compared directly to in-situ spacecraft measurements. We use magnetosphere-ionosphere (MI) coupling theory to calculate currents from the auroral brightness as measured with the Hubble Space Telescope and from plasma flow speeds measured in-situ with the *Galileo* spacecraft. The effective Pedersen conductance of the ionosphere (Σ_P^*) remains a free parameter in this comparison. We first show that the field-aligned currents per radian of azimuth calculated from the auroral observations, found to be $I_{||} = 9.54_{-6.35}^{+11.5}$ MA rad⁻¹ and $I_{||} = 10.64_{-6.11}^{+11.1}$ MA rad⁻¹ in the north and south, respectively, are consistent with previous results. Then, we calculate the Pedersen conductance from the combined datasets, and find it ranges from $0.02 < \Sigma_P^* < 2.26$ mho overall with averages of $0.14_{-0.08}^{+0.31}$ mho in the north and $0.14_{-0.09}^{+0.26}$ mho in the south. Taking the currents and effective Pedersen conductance together, we find that the average ME intensity and plasma flow speed in the middle magnetosphere (10-30 R_J) are broadly consistent with one another under MI coupling theory. We find evidence for peaks in the distribution of Σ_P^* near 7, 12, and 14 hours magnetic local time (MLT). This variation in Pedersen conductance with MLT may indicate the importance of conductance in modulating MLT- and local-time-asymmetries in the ME, including the apparent sub-rotation of some auroral features within the ME.

Plain Language Summary

The brightest part of Jupiter’s aurorae– the main emission– forms arcs of sheet-like lights surrounding both magnetic poles, similar to the Earth’s aurorae. At both planets, these lights are caused by charged particles flowing into the planet’s atmosphere, where they collide with gases and glow. At Jupiter, these particles are electrons which flow in electrical currents connecting the planet to the charged-particle-filled space surrounding it. Here, we use Hubble Space Telescope images of Jupiter’s aurorae spanning a decade to build up an average picture of the brightness and location of this main emission. The brightness is related to the energy of the electrons, which in turn is related to the strength of electrical currents flowing near the planet. We then use particle measurements made by the *Galileo* spacecraft in orbit around Jupiter to make an average picture of these particles as they move around Jupiter. These speeds are related to the same electrical currents, but include an electrical conductivity term describing how easily currents flow through Jupiter’s auroral atmosphere. We combine all these measurements to calculate the conductivity, and present results which are consistent with expectations but which fluctuate more quickly than expected in parts of the main emission.

1 Introduction

Jupiter’s ultraviolet (UV) auroral main emission (ME), typically the most powerful component of the planet’s large-scale auroral regions, takes the form of a partially-closed oval of auroral emission surrounding each of the planet’s magnetic poles. The Jovian aurorae are detectable at all local times (LT) including on the planet’s dayside (Clarke et al., 2004; Bonfond et al., 2017), where they are significantly brighter than Jupiter’s surface UV emission (Gustin et al., 2012) and can thus be observed routinely with the Hubble Space Telescope (HST). In the southern hemisphere, the ME forms a nearly circular curtain of light; however, the presence of multiple significant non-dipolar magnetic field components in the northern hemisphere complicates the structure, resulting in a characteristic ‘kidney bean’ shape (Grodent et al., 2008; Connerney et al., 2022), as shown by the HST observation and statistically-averaged reference main oval (‘statistical main oval’, or SMO) in Figure 1a.

65 The ME has historically been thought to originate from the magnetosphere-ionosphere
 66 (MI) coupling currents flowing in the Jovian middle magnetosphere, radially outward in
 67 the equatorial plasma disc, equatorward in the ionosphere, and along magnetic field lines
 68 between (Hill, 2001; Cowley & Bunce, 2001; Nichols & Cowley, 2003, 2004, 2005; Ray
 69 et al., 2010, 2014; Smith & Aylward, 2009; Tao et al., 2009). This current system arises
 70 from the azimuthal distortion (or ‘bendback’) of the field caused by the planet’s reser-
 71 voir of angular momentum opposing the decrease in angular velocity of flux tubes laden
 72 with Iogenic plasma as they diffuse radially outward. In the absence of torques, these
 73 diffusing flux tubes would tend to conserve angular momentum, resulting in a decrease
 74 in the angular velocity proportional to r^{-2} . The resultant lag in the flux tubes corre-
 75 sponds to an azimuthal bendback in the magnetic field structure and thus a loop of field-
 76 aligned current which acts to partially enforce the corotation of the plasma composing
 77 the plasma disk by exerting a $\mathbf{J} \times \mathbf{B}$ force in the direction of corotation. The strongest
 78 field-aligned currents occur near where rigid corotation breaks down (Hill, 1979; Nichols
 79 & Cowley, 2004). The ME current system is characterized primarily by the rapid ro-
 80 tation and strength of Jupiter’s magnetic field, rather than by solar influence as is the
 81 case in the Earth’s own magnetosphere and auroral ovals (Cowley & Bunce, 2001; South-
 82 wood & Kivelson, 2001), though solar wind influence is not completely absent (Kita et
 83 al., 2019; Nichols et al., 2017). These MI-coupling currents and the associated ME ovals
 84 are thus always present, owing to the continuous production of Iogenic plasma and dif-
 85 fusion of this plasma outward through the magnetosphere.

86 The production and diffusion of Iogenic plasma is not constant and the Jovian mag-
 87 netosphere is varies in System III (SIII) magnetic longitude (λ_{III}), local time (LT), and
 88 magnetic local time (MLT). This results in various asymmetries in the brightness, shape,
 89 distribution, and dynamics of auroral forms within the ME oval. The southern ME is
 90 brighter on average than the northern (Gérard et al., 2013) and the dusk side of the ME
 91 is brighter on average than dawn, an effect which is amplified in the brighter southern
 92 hemisphere (Bonfond et al., 2015). On occasions where the dawn side is brighter than
 93 dusk, an exceptionally bright auroral feature— a dawn storm, perhaps— is typically lo-
 94 cated on the dawn ME (Gérard, Grodent, et al., 1994; Bonfond et al., 2021; Rutala et
 95 al., 2022). While the locations of the ME remain fixed in SIII longitude and latitude (Clarke
 96 et al., 2004; Gérard, Dols, et al., 1994; Grodent et al., 2003), auroral features on the ME
 97 may subcorotate, lagging behind the rigid corotation rate of the planet. Subcorotation
 98 occurs more often in the dawn sector than the noon and dusk sectors (Rutala et al., 2022),
 99 an effect which appears to be separate from the appearance of bright dawn storms. Ad-
 100 ditional subcorotating auroral forms, the ME auroral discontinuity (Radioti et al., 2008)
 101 and small-scale brightening (Palmaerts et al., 2014) are observed localized near noon.
 102 The dusk side of the ME as viewed from the Earth is typically wider and more diffuse
 103 than near dawn (Gérard, Dols, et al., 1994); this asymmetry is larger in the northern hemi-
 104 sphere, where the northern magnetic anomaly is typically located in remote observations
 105 (Grodent et al., 2008). This asymmetry was originally considered to be a variation in
 106 local time (Caldwell et al., 1992), before improved HST observations made it appear to
 107 be a variation in SIII longitude (Gérard, Dols, et al., 1994). Recent *Juno* observations
 108 of the ME oval morphology indicate that this asymmetry may vary in a more complex
 109 way, dependent on both local time and SIII longitude (Greathouse et al., 2021).

110 These phenomena have generally been thought to arise from deviations from the
 111 ideal axisymmetric MI-coupling theory previously discussed. However, predictions of
 112 this theory are not always in accordance with observations, raising the possibility that
 113 the MI-coupling theory itself only partially describes the generation of the ME oval at
 114 Jupiter (Bonfond et al., 2020). Mean field-aligned MI-coupling currents of 58 MA and
 115 24 MA in the southern and northern ME regions, respectively, have been derived from
 116 *Juno* measurements, reflecting the observed north-south brightness asymmetry of the
 117 ME ovals (Kotsiaros et al., 2019). These currents appear in primarily longitudinal, though
 118 variable, sheets in keeping with the schematic picture of MI coupling theory. Further *Juno*

119 measurements have found that the field lines associated with ME aurorae host precip-
 120 itating electrons, as required to drive field-aligned currents, along with bi-directional elec-
 121 tron distributions (Mauk et al., 2017, 2018), suggesting that additional auroral emission
 122 zones, co-located or nearly co-located with the ME, may be driven by acceleration pro-
 123 cesses other than field-aligned potentials (Mauk et al., 2020). The measured bi-directional
 124 electron distributions may, however, be a secondary effect, driven by the flow of intense
 125 field-aligned currents (Nichols & Cowley, 2022). The equatorial radial currents derived
 126 from *Juno* magnetometer measurements are highly correlated with simultaneous HST
 127 observations of the dawnside ME auroral intensity (Nichols & Cowley, 2022). On large
 128 scales, the MI-coupling theory still explains the bulk of the observed variation in ME au-
 129 roral brightness, including during short-term enhancements (Nichols et al., 2020).

130 A further discrepancy between the modeled and observed auroral MI-coupling sys-
 131 tem at Jupiter lies in the auroral brightness asymmetry across the dayside ME. While
 132 the dusk side of the ME oval is typically observed to be brighter than the dawn side (Bonfond
 133 et al., 2015), models predict that this asymmetry should be reversed owing to the larger
 134 field bend-back in the dawn sector (Ray et al., 2014). Field bend-back is strongly cor-
 135 related with ME auroral brightness, particularly near dawn (Nichols & Cowley, 2022).
 136 Field bend-back is caused by angular plasma flow speeds in the middle magnetosphere
 137 slower than the rotation rate of the planet, or subcorotation relative to the planet’s ro-
 138 tation, so in considering only the quasi-steady-state MI coupling current system, an an-
 139 tycorrelation between the degree of field bend-back and plasma angular velocity is ex-
 140 pected (Bonfond et al., 2020). A partial ring current, spanning the nightside middle mag-
 141 netosphere with a source near dusk and a sink near dawn (Walker & Ogino, 2003) may
 142 ease this tension if the ring current closes along field-aligned currents, decreasing the ef-
 143 fective field-aligned currents near dawn and increasing them near dusk (Bonfond et al.,
 144 2015). On top of this effect, careful consideration is required to relate instantaneous, in-
 145 situ measurements of plasma velocity to the measurement of magnetic field bend-back
 146 in a dynamic region of the magnetosphere such as the dawn sector. The anticorrelation
 147 between field bend-back and plasma velocity is only maintained in the quasi-steady-state
 148 scenario. If magnetospheric plasma near dawn is rapidly accelerated, the measured plasma
 149 velocity may be high despite large degrees of field bend-back, as the plasma and field lines
 150 have yet to “catch up” to corotational velocity. This scenario matches observations of
 151 both the plasma (Krapp et al., 2001; Bagenal et al., 2016) and the magnetic field (Khurana
 152 & Schwarzl, 2005) near dawn. Such a sudden acceleration of the middle magnetospheric
 153 plasma may be driven by an equally sudden increase in the conductance of the MI-coupling
 154 circuit, as is the case near the dawn terminator where the previously-unlit ionosphere
 155 is re-photoionized by solar extreme ultraviolet (EUV) light (Tao et al., 2010). This sce-
 156 nario has been suggested to explain the apparent subcorotation of some auroral forms
 157 relative relative to the SMO in the dawn sector (Rutala et al., 2022), and will be explored
 158 here in more detail.

159 Here, we present the first large-scale statistical survey of the typical HST-observed
 160 ME brightness, spanning more than 10 years and 200 cumulative hours of exposure time.
 161 The ME brightness is mapped from the polar ionosphere out into the magnetospheric
 162 equatorial plane and averaged in bins defined by MLT, equatorial radial distance (ρ_e),
 163 and the solar central meridian longitude (solar CML), so that variations relative to MLT
 164 and λ_{III} can be differentiated. From these binned values, the associated maximum field-
 165 aligned current density and total currents under MI-coupling theory are derived. We com-
 166 pare the derived total currents from this novel analysis of HST observations to litera-
 167 ture values, finding good agreement in scale. These values are then compared to non-
 168 contemporaneous in-situ *Galileo* Plasma Science (PLS) measurements of the plasma flow
 169 speed and associated field-aligned current density and total current binned in the same
 170 way as the HST observations in order to perform a superposed epoch analysis. Finally,
 171 we compare the HST- and *Galileo*- derived currents directly, assuming that they fully
 172 describe the large-scale, time-averaged state of the MI-coupling system, to derive a dis-

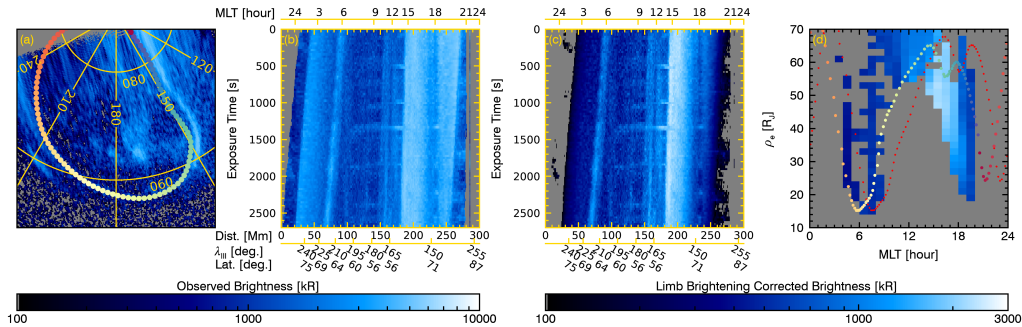


Figure 1. Plots showing multiple views of Jupiter’s northern ME on May 22, 2016 beginning at 18:02:46 UTC, as observed with HST STIS. Panel (a) shows a top-down, polar view of the northern ME, with the statistical main oval (SMO) shown with a red dashed line and λ_{III} and latitude graticules in yellow. Panel (b) shows a labeled keogram, where the observation in (a) is represented in the first (top) row. The values in both (a) and (b) are log-scaled with colors corresponding to the colorbar beneath. Panel (c) depicts the same keogram, but with a limb-brightening correction applied. Panel (d) shows the corrected keogram projected to the magnetospheric equatorial plane as a function of MLT and ρ_e , with the projected SMO corresponding to the first (dashed) and final (dotted) exposures shown in red. The values in both (c) and (d) are log-scaled, with colors corresponding to the separate colorbar beneath.

173 tribution of the Pedersen conductance in MLT, ρ_e , and solar CML. The resulting con-
 174 ductance distribution is additionally mapped back into the ionosphere. We find that the
 175 Pedersen conductance peaks in the dawn sector, and varies primarily in MLT, consis-
 176 tent with controlling the subcorotation of auroral forms in the dawn ME and helping re-
 177 solve the tension between high degrees of field bend-back and high plasma velocities in
 178 the dawn sector.

179 2 Data

180 2.1 Hubble Space Telescope Data

181 Archival observations of Jupiter’s ultraviolet (UV) aurorae made with the Advanced
 182 Camera for Surveys Solar Blind Channel (ACS/SBC) and Space Telescope Imaging Spec-
 183 trograph (STIS) on HST were obtained for this study. These observations comprise more
 184 than 200 cumulative hours of exposure, and span 2007 and 2016–2019; this large sur-
 185 vey is expected to be representative of the general state of Jupiter’s main emission au-
 186 rorae. Further details about this set of observations are presented in Rutala et al. (2022)
 187 and references therein.

188 Time-tagged STIS observations were split into non-overlapping 30s intervals to cre-
 189 ate images, while the typical ~ 100 s exposures for the ACS observations were unchanged.
 190 Images were reduced and projected onto an equirectangular planetocentric grid using the
 191 standard procedures in the Boston University HST data reduction pipeline (Clarke et
 192 al., 2009; Nichols & Cowley, 2022; Rutala et al., 2022, e.g.); the projection from the HST
 193 perspective to an equirectangular grid allows the observations to be viewed from any per-
 194 spective, as illustrated by the reduced observation mapped to an orthographic polar view
 195 in Figure 1a. The factors used to convert the observed auroral brightness from counts/s
 196 to kR of unabsorbed H and H₂ emission vary with color ratio (Gustin et al., 2012), which
 197 can change rapidly on both small and large scales. Here, we estimate an effective value
 198 of the color ratio of 12 in the ME region from *Juno* ultraviolet spectrograph (UVS) based

199 maps of the color ratio distribution (Gérard et al., 2018). Auroral intensities in the ACS/SBC
 200 images were further multiplied by a factor of 1.4 for those using the F115LP filter and
 201 1.6 for those using the F125LP filter, following recent changes to the SBC absolute flux
 202 calibration (Avila et al., 2019).

203 In each reduced image, an ME brightness profile is measured as the mean bright-
 204 ness of the brightest quartile of emission within $\pm 5^\circ$ perpendicular to the SMO, as found
 205 by Nichols et al. (2009), in steps along the ME. 300 steps evenly spaced in distance along
 206 the SMO with dynamic sizes were found to maximize resolution while preventing over-
 207 lap between pixels sampled by adjacent steps. The extracted brightness profile is stacked
 208 into a keogram for each image within the same HST visit, and aligned such that the loca-
 209 tion along the SMO is measured horizontally and exposure time is measured vertically.
 210 Figure 1b shows a keogram created in part from the observation in Figure 1a, with SIII
 211 coordinates, distance along the SMO, and MLT all labeled. Limb-brightening correction
 212 factors found as the inverse cosine of the view angle (Grodent et al., 2005) were applied
 213 to each keogram, the results of which are demonstrated in Figure 1c. The inverse-cosine
 214 correction generally overestimates the limb-brightening effect very near the edge of planet’s
 215 disk as viewed by HST. The effect of this overestimation is partially countered by remov-
 216 ing all parts of the observations within 10° of the limb; the slight remaining effects of
 217 the overestimation will be discussed in the Results. The keogram production process is
 218 further discussed in Rutala et al. (2022).

219 In each of the 288 keograms, the auroral brightness (I), local time (LT), latitude
 220 (ϕ), System III longitude (λ_{III}), and the 1σ width ($\delta\theta$) of the ME were recorded for ev-
 221 ery pixel. Pixels were then mapped from λ_{III} and ϕ in the ionosphere to magnetic lo-
 222 cal time (MLT) and radial distance in the equatorial plane of the magnetosphere (ρ_e)
 223 using the magnetic flux equivalence mapping of Vogt et al. (2011). The internal mag-
 224 netic field for the mapping was specified to be the JRM09 magnetic field model (Connerney
 225 et al., 2018) which, over the spatial scales relevant here, is very similar to the more re-
 226 cent JRM33 model (Connerney et al., 2022). Solar CML values for the mapping were
 227 found using ephemerides from the NASA NAIF SPICE toolkit (Acton et al., 2018). The
 228 angular width of the ME, $\delta\theta$, was mapped to a radial width, $\delta\rho_e$, in the same manner.
 229 The observed and mapped parameters were then binned by 1 hour in MLT, $2 R_J$ in ρ_e ,
 230 and 24° in solar CML; a typical, 40 minute HST observation of the Jovian aurorae spans
 231 $\sim 24^\circ$ of longitude as the planet rotates. Values in each bin were calculated as the arith-
 232 metic mean. Figure 1d shows the auroral brightness of the keogram in Figure 1c binned
 233 in MLT and ρ_J , with the projected SMO locations corresponding to the first and last
 234 exposures included for reference. As Figure 1d represents a ~ 40 min. observation, it
 235 effectively spans a single bin in solar CML and can as such be binned in MLT and ρ_e
 236 and displayed completely in two dimensions. Emissions mapping to radial distances less
 237 than that of SMO originate at lower latitudes than the SMO, as is the case particularly
 238 near dusk in Figure 1. The binned distributions of auroral brightness and number of
 239 observations per bin are shown in full in Figure 2; to display these distributions, which
 240 are binned in three-dimensional, each panel in Figure 2 represents the two-dimensional
 241 distribution with respect to MLT and ρ_e corresponding to a single solar CML bin.

242 2.2 *Galileo* PLS Measurements

243 Plasma parameters derived from the numerical moments of *Galileo* PLS real-time
 244 science data were obtained, as calculated by Frank et al. (2023). The *Galileo* spacecraft’s
 245 native Inertial Rotor Coordinate (IRC) system, a despun coordinate system based on
 246 the spacecraft’s geometry, is complex (Bagenal et al., 2016) and has not been fully im-
 247 plemented into SPICE (Acton et al., 2018), due in part to the *Galileo* spacecraft her-
 248 itage predating the SPICE toolkit. SPICE ephemerides for the *Galileo* spacecraft po-
 249 sition are available for all 6751 moments; spacecraft pointing information is only avail-
 250 able for 4897 of those 6751. So that the full set of moments can be used, the plasma flow

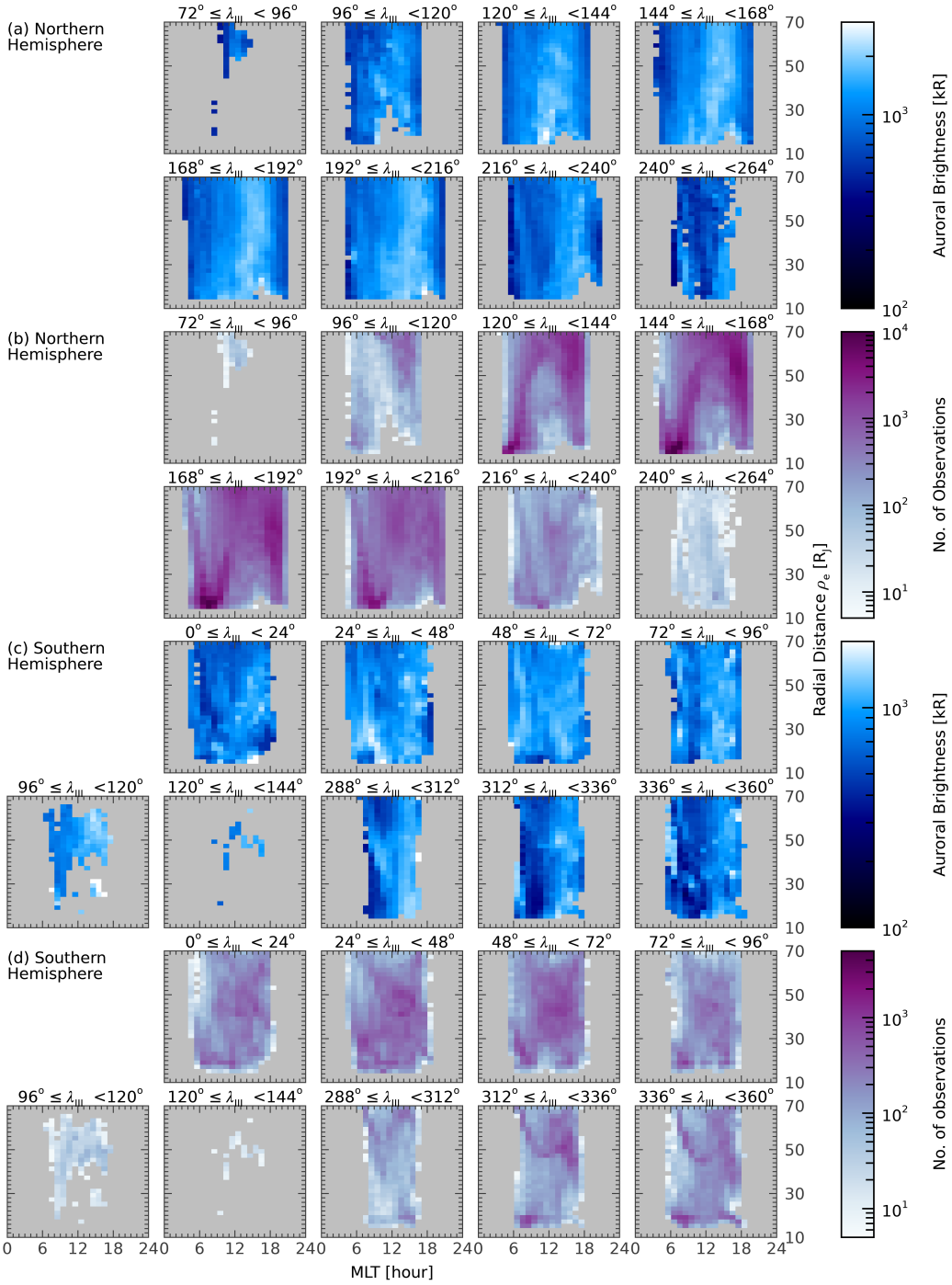


Figure 2. Two-dimensional distributions of the (a,c) auroral brightness and the (b, d) number of observations for both the (a, b) northern and the (c, d) southern hemispheres, with colors for each MLT- ρ_e bin corresponding to the colorbars to the right of each set of panels. Each distribution is labeled with the range of solar CMLs it spans; solar CML ranges for which there are no observations were excluded. In the sample analyzed here, it is evident that the northern hemisphere is typically brighter than the southern and that dusk is typically brighter than dawn.

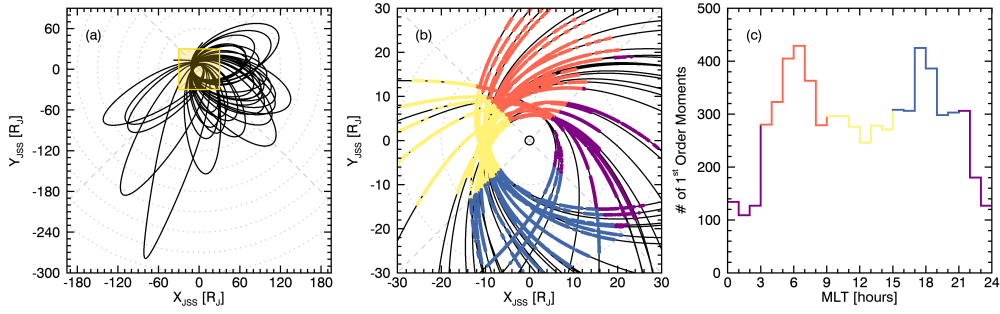


Figure 3. Plots illustrating *Galileo* PLS coverage of the magnetosphere. Plot (a) shows all 34 *Galileo* orbits projected into Jupiter’s equatorial plane in the Jupiter-Despun-Sun (JSS) reference frame, with the region spanning $\pm 30R_J$ in both dimensions highlighted in yellow. (b) A zoomed-in view of the highlighted region in (a), with individual *Galileo* PLS plasma flow speed measurements overplotted as points, colored according to MLT sector: dawn ($03 \leq \text{MLT} < 09$) in orange, noon ($09 \leq \text{MLT} < 15$) in yellow, dusk ($15 \leq \text{MLT} < 21$) in blue, and mid-night ($00 \leq \text{MLT} < 03$; $21 \leq \text{MLT} < 24$) in purple. (c) A histogram of the number of *Galileo* PLS plasma flow speed measurements in each hour-wide MLT bin. The abundance of dawn and dusk observations, compared to those near noon and particularly near midnight, is evident.

251 speed is estimated as the root-sum-square of all the velocity components, as the azmi-
 252 thal component of the plasma velocity is expected to be much larger than the radial
 253 and polar components.

254 These numerical moments span 31 of *Galileo*’s 34 orbits, and cover a combined 129
 255 days. The plasma parameters span $10R_J \leq \rho_e \leq 30R_J$ within $\sim 1 - 2R_J$ of the equa-
 256 torial plane, with larger distances from the equatorial plane corresponding to larger ra-
 257 dial distances. These parameters cover all local times and SIII longitudes, with a bias
 258 in local time sampling towards dawn and dusk. Figure 3 illustrates the coverage of the
 259 numerical moments relative to *Galileo*’s full orbit and shows this bias. Figures 3a and
 260 3b are plotted in the Jupiter-De-Spun-Sun (JSS) reference frame, which is defined to have
 261 \hat{Z} aligned with Jupiter’s rotational axis, the Sun located in the $\hat{X} - \hat{Z}$ plane, and \hat{Y}
 262 completing the right-hand orthogonal set. The average plasma corotation rate (R_C) was cal-
 263 culated for bins spanning 1 hour in MLT and $2 R_J$ in ρ_e ; as the middle magnetosphere
 264 is dominated by magnetic local time effects rather than longitudinal effects (Vogt et al.,
 265 2011; Ray et al., 2014), the *Galileo* data were not binned by the solar CML of the planet.
 266 Binning of the plasma parameters was performed by averaging with weights proportional
 267 to the inverse of the parameter variance to be representative of the time-averaged MI-
 268 coupled system.

269 The plasma corotation rate R_C is defined as

$$270 \quad R_C = \frac{v_{flow}}{\rho_e \Omega_J} = \frac{\omega_{flow}}{\Omega_J} \quad (1)$$

271 where v_{flow} is the calculated linear plasma flow velocity from the *Galileo* PLS data, ω_{flow}
 272 is the angular plasma flow velocity ($\omega_{flow} = v_{flow}/\rho_e$), and Ω_J is the angular vel-
 273 ocity at which Jupiter rotates ($1.76 \times 10^{-4} \text{ rad s}^{-1}$). R_C is averaged in each bin rather
 274 than v_{flow} to account for the expected inverse relationship between equatorial distance
 275 ρ_e and v_{flow} . When $v_{flow} = \rho_e \Omega_J$, the plasma is rigidly corotating with the planet and
 276 $R_C = 1$. In turn, when $v_{flow} = 0$ then the plasma is fixed with respect to the Sun-

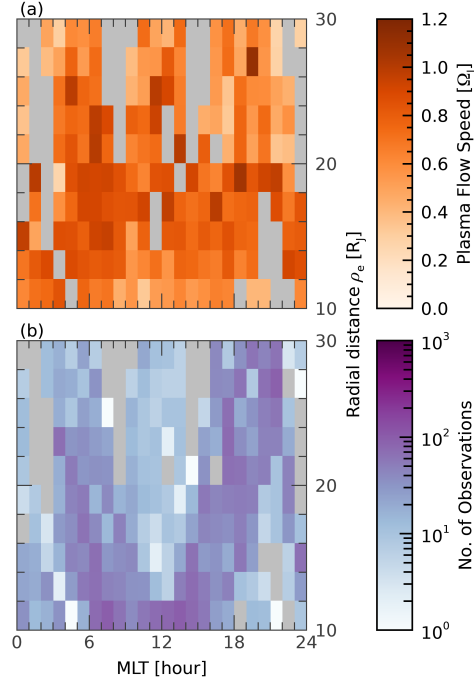


Figure 4. Two-dimensional distributions of the (a) corotation rate (R_C) of the equatorial plasma from *Galileo* PLS moments from Equation 1 and the (b) number of moments. The moments were not binned with respect to solar CML, as the middle magnetosphere is expected to vary primarily in MLT.

277 Jupiter geometry, or effectively fixed in MLT, and $R_C = 0$. The full set of 6751 plasma
 278 parameters used from *Galileo* PLS are summarized in Figure 4, which shows the two-
 279 dimensional distributions of the corotation rate R_C and the number of moments N with
 280 respect to MLT and ρ_e .

281 3 Analysis

The field-aligned current per radian of azimuth, $I_{||}$, in the coupled MI system driv-
 ing Jupiter’s main emission near the ionosphere can be found as

$$I_{||} = -2 \int_0^{\rho_e} j_z \rho'_e d\rho'_e \quad (2)$$

$$= 4\Sigma_P^* \Omega_J (1 - R_C) F_e \quad (3)$$

282 adapted from Equation 16 in Cowley and Bunce (2001). Here j_z is the field-aligned cur-
 283 rent density flowing out of the current sheet lying in the middle magnetosphere’s equa-
 284 torial region, Σ_P^* is the height-integrated effective Pedersen conductance, $\Omega_J = 1.76 \times$
 285 10^{-4} rad s $^{-1}$ and R_C are the angular velocity and magnetospheric plasma corotation rates
 286 defined previously, and F_e is the equatorial flux function, a function which maps the au-
 287 roral ionosphere to the equatorial middle magnetosphere along contours of constant mag-
 288 netic flux. The field-aligned current per radian of azimuth $I_{||}$ can be calculated from the
 289 auroral brightness observed with HST using Equation 2 and from the plasma flow speed
 290 derived from *Galileo* PLS using Equation 3, as will be discussed in Sections 3.1 and 3.2,
 291 respectively.

292

3.1 Field-aligned currents from HST observations

The brightness of the ME aurorae observed with HST is directly proportional to the precipitated energy flux of auroral electrons E_f incident on the atmosphere, with a conversion factor of 10 kR per 1 mW m⁻² (Gustin et al., 2012; Nichols & Cowley, 2022). This energy flux E_f is in turn related to the field-aligned current density just above the auroral ionosphere $j_{||}$ as

$$j_{||} = j_{||,0} \left(\pm \sqrt{2 \frac{E_f}{E_{f,0}} - 1} \right) \quad (4)$$

293

294

295

296

297

298

299

300

301

302

303

304

where $j_{||,0}$ is the maximum field-aligned current density above the ionosphere and $E_{f,0}$ is the maximum precipitated energy flux of auroral electrons, both for the case of an absence of field-aligned potentials. Equation 4 is derived by assuming the minimum necessary field-aligned potentials for currents to flow into the ionosphere. The maximum energy flux in the absence of field-aligned potentials is $E_{f,0} = 2N\sqrt{W_{th}/2\pi m_e}W_{th}$ (Equation 37 in Cowley and Bunce (2001)), which is a number flux of electrons ($2N\sqrt{W_{th}/2\pi m_e}$) multiplied by a characteristic energy (W_{th}). $E_{f,0}$ can therefore be estimated by measurable physical parameters; here, $N = 0.018 \text{ cm}^{-3}$ (Bagenal et al., 2016; Huscher et al., 2021) and $W_{th} = 5 \text{ keV}$ (Allegrini et al., 2021) are used. Similarly, the maximum field-aligned current density just above the ionosphere in the absence of field-aligned potentials is $j_{||,0} = eN\sqrt{W_{th}/2\pi m_e}$, the number flux of electrons multiplied by e , the elementary charge (Equation 28 in Cowley and Bunce (2001)).

305

306

307

308

309

310

311

312

313

314

315

316

317

318

319

320

The quantity j/B is constant along a magnetic field line provided there are no field-perpendicular currents intersecting the field line outside of the equatorial and ionospheric regions (Cowley & Bunce, 2001), so $j_{||}$ can be written as $j_z B_i / B_e$, where B_i and B_e are the strengths of the magnetic field along the field line in the ionosphere and the current sheet in the equatorial plane, respectively. The magnetic field strength in the equatorial plane of the magnetosphere B_e , is calculated from the form provided in Vogt et al. (2011), which is itself a fit to in-situ magnetic field measurements from *Pioneer 10*, *Pioneer 11*, *Voyager 1*, *Voyager 2*, *Ulysses*, and *Galileo* spanning 20–120R_J. The magnetic field strength in the ionosphere was found using the internal magnetic field model based on *Juno*'s first 33 orbits of Connerney et al. (2022) (henceforth, JRM33), calculated to order 13 using the code provided by Wilson et al. (2023), and assuming an altitude of 1R_J. The magnetic field function of Vogt et al. (2011) is more appropriate for B_e than the more recent JRM33 model as it captures the significant variation of the middle and outer magnetosphere with MLT; beyond 10R_J, the higher order terms in the JRM33 model become negligible and the resulting field is very nearly dipolar and azimuthally symmetric.

Equation 4 can thus be substituted into Equation 2 for j_z to give

$$I_{||} = -2 \int_0^{\rho_e} j_{||,0} \frac{B_e}{B_i} \left(\pm \sqrt{2 \frac{E_f}{E_{f,0}} - 1} \right) \rho'_e d\rho'_e \quad (5)$$

321

322

323

324

325

326

327

328

329

330

331

332

which can be used to calculate the field-aligned current per radian of azimuth $I_{||}$ corresponding to a given auroral brightness. Evaluation of Equation 5 requires an integrable auroral electron energy flux $E_f(\rho'_e)$, which in turn requires a function of the auroral brightness over equatorial distance. The variation of the auroral brightness with equatorial distance illustrated in Figure 2 does not represent this function directly. Instead, these distributions show the typical values of the observed ME when the ME maps to a given location in MLT- ρ_e space, which in turn represents the maximum of the field-aligned current density j_z for a given span of solar CML. An integrable radial distribution of $E_f(\rho'_e)$ is therefore approximated as a Gaussian having a peak value of E_f , a center defined by the corresponding radial bin, and a width defined by the angular width of the ME ($\delta\theta$) magnetospherically mapped to a radial width ($\delta\rho_e$). The resulting radial distributions are then numerically integrated from 0 out to the corresponding ρ_e value.

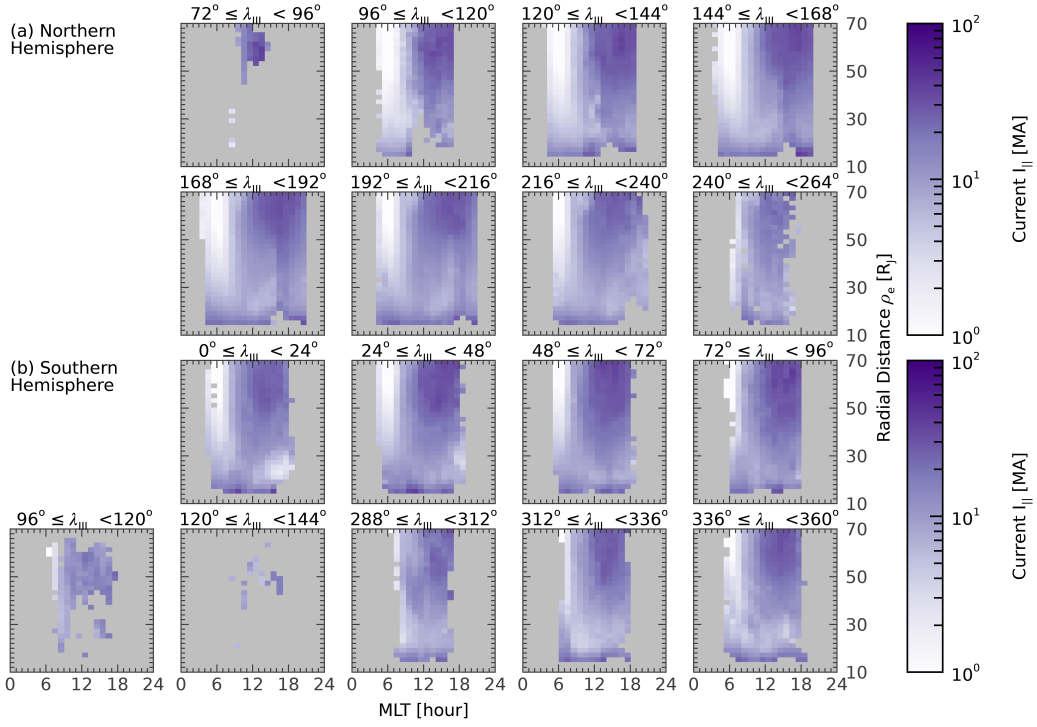


Figure 5. Two-dimensional distributions of the integrated field-aligned current per radian of azimuth ($I_{||}$ calculated from Equation 5 for the (a) northern and (b) southern hemispheres, with colors for each MLT- ρ_e bin corresponding to the colorbars to the right. Each distribution is labeled with the range of solar CMLs it covers. Generally, stronger currents are seen to occur at dusk rather than dawn, and when the magnetosphere is more perturbed (i.e., when the ME maps to more distant regions of the magnetosphere).

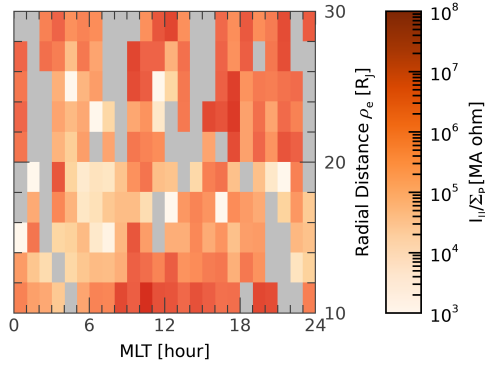


Figure 6. Two-dimensional distribution of the quantity I_{\parallel}/Σ_P^* derived from the *Galileo* PLS moments using Equation 6, with colors in each MLT- ρ_e bin corresponding to the colorbar to the right. Generally, I_{\parallel}/Σ_P^* is seen to be smaller at dawn than at dusk.

333 The resulting values of I_{\parallel} we report are thus average field-aligned currents per radian
 334 of azimuth entering the ionosphere at the ME, when the location of the ME maps to the
 335 current sheet at the location specified by the corresponding bin. The distributions of I_{\parallel}
 336 with MLT, ρ_e , and solar CML in Figure 5 thus illustrate various independent MI cou-
 337 pling configurations rather than multiple samples of the same configuration. To clarify
 338 further, the distributions of I_{\parallel} calculated here are not expected to increase monoton-
 339 ically with equatorial distance ρ_e , even though the integral of $F_e(\rho_e')$ would, for the same
 340 reasons that the ME brightness does not increase monotonically with ρ_e in Figure 2.

341 3.2 Field-aligned currents from Galileo-PLS data

Returning to Equation 3 and rearranging, the total field-aligned current per radian
 of azimuth I_{\parallel} flowing into the ionosphere divided by the effective, height-integrated Ped-
 ersen conductance Σ_P^* of the ionosphere, can be found as

$$\frac{I_{\parallel}}{\Sigma_P^*} = 4\Omega_J(1 - R_c)F_e \quad (6)$$

342 The height-integrated effective Pedersen conductance Σ_P^* is the sum of all conductance
 343 terms and is reduced from the true value, Σ_P , by a factor of $(1-k)$ to account for the
 344 slippage in the ion-neutral coupling in the ionosphere. The values of k range from $0 <$
 345 $k < 1$, with $k = 0$ corresponding to no slippage of the neutral atmosphere relative to
 346 the planet's rigid rotation rate and $k \approx 1$ corresponding to maximal slippage (Huang
 347 & Hill, 1989; Nichols & Cowley, 2003). The equatorial flux F_e , which relates locations
 348 in the ionosphere to conjugate points in the current sheet in the equatorial plane of the
 349 magnetosphere along contours of constant magnetic flux, is a function of both MLT and
 350 ρ_e and is calculated using the form provided by Ray et al. (2014). This description of
 351 $F_e(\text{MLT}, \rho_e)$ is based on a slightly modified version of the empirical magnetic field model
 352 used to map HST observations into the equatorial magnetospheric plane (Vogt et al., 2011).
 353 The differences between this and the unmodified empirical magnetic field model are great-
 354 est near the planet; the two descriptions agree throughout the middle magnetosphere where
 355 MI coupling currents flow, ensuring consistency between the values derived from *Galileo*
 356 PLS and HST observations.

357 The quantity I_{\parallel}/Σ_P^* can thus be solved for using *Galileo* PLS-derived values of the
 358 plasma corotation rate R_c and the known form of F_e . This quantity is introduced for
 359 convenience and has limited physical meaning, despite having the form of an electric po-

360 tential. Instead, the quantity $I_{||}/\Sigma_P^*$ groups unknown parameters together, and will al-
 361 low further exploration of the distribution of Σ_P^* when compared to the values of $I_{||}$ de-
 362 rived from HST observations. Figure 6 shows the distributions of the quantity $I_{||}/\Sigma_P^*$
 363 with MLT and equatorial distance ρ_e .

364 4 Results and Discussion

365 4.1 Azimuthally integrated field-aligned currents

366 First, we focus on the field-aligned current per radian azimuth $I_{||}$ derived from HST
 367 observations, which, unlike the parameter $I_{||}/\Sigma_P^*$ derived from *Galileo* measurements,
 368 is representative of the field-aligned auroral currents flowing in Jupiter’s coupled MI sys-
 369 tem without any further assumptions about the ionospheric Pedersen conductance. The
 370 northern ME is found to have a median current per radian of azimuth of $I_{||} = 9.54^{+11.5}_{-6.35}$
 371 MA rad⁻¹, while the southern ME has a median current per radian of azimuth of $I_{||} =$
 372 $10.6^{+11.1}_{-6.11}$ MA rad⁻¹. These median values are found using a Monte Carlo bootstrap anal-
 373 ysis with lognormal error perturbation (henceforth just “medians”), in order to better
 374 account for the measurement errors in the non-Gaussian distribution of currents (Curran,
 375 2014). Upper and lower errors correspond to the 84th and 16th percentiles, respectively,
 376 to approximate 1σ errors. These median currents are in very good agreement with the
 377 currents calculated from *Juno* magnetometer measurements, both lying within the ~ 1 –
 378 27 MA rad⁻¹ range of $I_{||}$ (Nichols & Cowley, 2022) and reproducing the magnitude, af-
 379 ter accounting for integration over azimuth, and North-South asymmetry previously mea-
 380 sured (Kotsiaros et al., 2019).

381 4.2 Effective Pedersen conductance

382 The effective Pedersen conductance (Σ_P^*) can be calculated by dividing the field-
 383 aligned current per radian of azimuth derived from HST measurements ($I_{||}$) by the quan-
 384 tity derived from *Galileo* PLS moments ($I_{||}/\Sigma_P^*$). Figure 7 shows distributions of this
 385 calculated effective Pedersen conductance for the northern and southern hemispheres;
 386 these plots are limited to $10 < \rho_e \leq 30R_J$ due to the coverage of the *Galileo* PLS moments.
 387 The binned distributions of $I_{||}/\Sigma_P^*$ are assumed to be the same at all solar CML in this
 388 analysis. We find 95% of conductances lie in the range $0.03 < \Sigma_P^* < 1.79$ mho in the north
 389 with a median of $\Sigma_P^* = 0.14^{+0.31}_{-0.08}$ mho and $0.02 < \Sigma_P^* < 2.26$ mho in the south with a
 390 median of $\Sigma_P^* = 0.14^{+0.34}_{-0.09}$ mho, with errors corresponding to the 16th and 84th percentiles.
 391 These averages are comparable to both theoretical estimates (Millward et al., 2002, 2005)
 392 and recent estimates made using *Juno* ultraviolet spectrograph (UVS) measurements and
 393 ionospheric modeling (Gérard et al., 2020, 2021) of $\Sigma_P \approx 0.5$, considering that these
 394 reported values are not reduced by the $(1 - k)$ factor. For typical values of $k \approx 0.4$ –
 395 0.7 (Millward et al., 2005), the novel method used here to calculate the conductance of
 396 the auroral ionosphere is in good agreement with literature values.

397 For clarity, Figure 8 shows the same data as Figure 7, but with the medians and
 398 the 84th/16th percentile errors of the effective Pedersen conductance in each bin plot-
 399 ted. By comparison to the average values and errors for each hemisphere overall, the vari-
 400 ations in conductance with respect to each binning parameter can be seen. Figures 8c
 401 and 8f show that Σ_P^* varies minimally with solar CML. Figures 8b and 8e show that the
 402 effective Pedersen conductance is generally higher at smaller radial values, correspond-
 403 ing to higher field-aligned currents when the magnetosphere is in a disturbed enough state
 404 for the ME to map to these distances. The conductance thus increases with current, as
 405 expected (Nichols & Cowley, 2004). The bin-to-bin variation is greatest when the con-
 406 ductance is interpreted as a function of MLT, as shown in Figures 8a and 8d. This sig-
 407 nificant variation in effective conductance with MLT is more likely than the variations
 408 with equatorial distance or solar CML to be related to the local time asymmetries in the
 409 appearance, distribution, and motion of ME aurorae. Both hemispheres display peaks

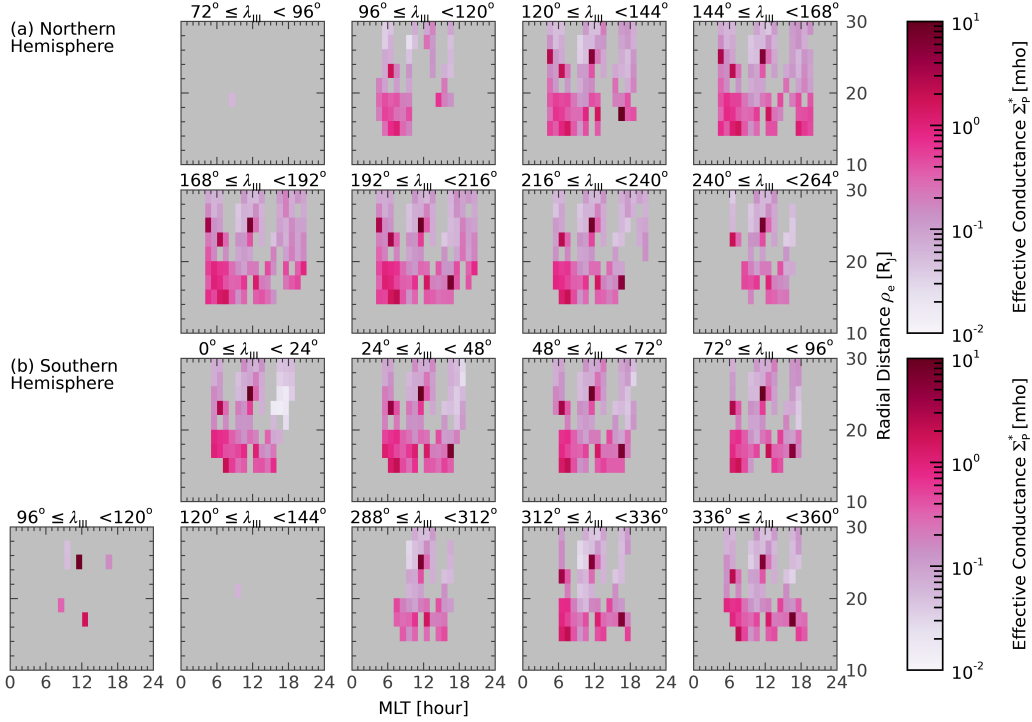


Figure 7. Two-dimensional distributions of the effective Pedersen conductance Σ_P^* for the (a) northern and (b) southern hemispheres, with the color of each MLT- ρ_e bin corresponding to the colorbars to the right. The effective Pedersen conductance is only calculated where both HST-derived and *Galileo* PLS-derived data are present. Generally, the conductance is greatest at smaller radial distances and nearer dawn.

410 in the effective conductance between 7–8, 12–13, and 14–15 MLT. It is worth not-
 411 ting that, without the limb-brightening correction applied to HST-observed aural bright-
 412 ness, derived field-aligned currents would be increased more near dawn and dusk than
 413 near noon, and Σ_P^* would increase proportionally. The overestimation of the limb-brightening
 414 correction factors thus results in an underestimation of the conductance near the planet’s
 415 limbs at dawn and dusk, and a more accurate model of Jupiter’s limb-brightening would
 416 heighten the peak in Σ_P^* between 7–8 MLT further than the others.

417 Figure 9 shows the complete conductance distributions mapped onto Jupiter’s aural
 418 ionosphere for each solar CML bin, allowing the variation in Σ_P^* with local time
 419 and location relative to the SMO to be visualized. The generally increased effective Ped-
 420 ersen conductance near local dawn, located to the left of each frame in Figure 9, is evi-
 421 dent. The smooth decrease in Σ_P^* with increasing ρ_e can be seen as a decrease in Σ_P^*
 422 with increasing latitude, particularly in the noon and dusk sectors, in Figure 9a. The
 423 same trend is not seen in Figure 9b, as the middle magnetosphere maps to a smaller range
 424 of latitudes in the southern ME than in the northern ME.

425 From the derived distributions of Σ_P^* alone, we cannot determine the cause of the
 426 variation of the conductance with MLT. It is of interest, however, that the effective Ped-
 427 ersen conductance peaks in the late-dawn (7–8 MLT) and noon (12–13 MLT) re-
 428 gions are generally collocated with known subcorotating emission features within the ME:
 429 the dawn storms and associated, less bright subcorotating emission features in the post-

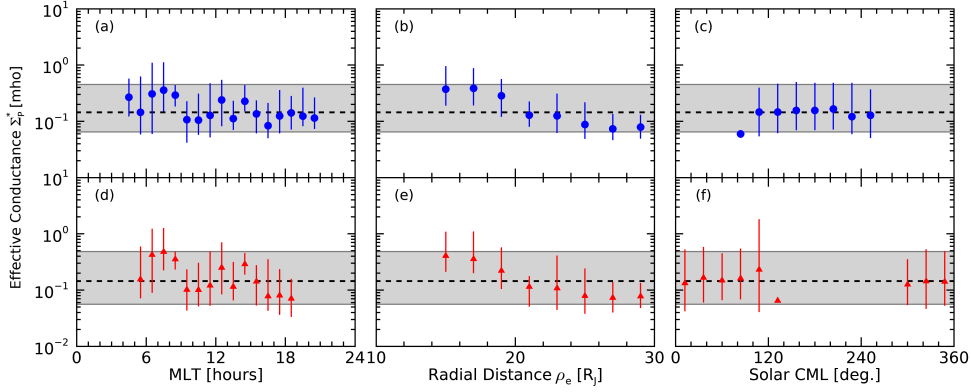


Figure 8. Plots showing the trends in the median effective Pedersen conductance Σ_P^* with MLT (a, d), ρ_e (b, e), and solar CML (c, f) for the northern (a, b, c; blue circles) and southern (d, e, f; red triangles) hemisphere ME. The conductance varies widely with MLT and insignificantly with solar CML.

dawn region (Rutala et al., 2022) and the noon discontinuity and auroral spot near noon (Radioti et al., 2008; Palmaerts et al., 2014).

The co-occurrence of increased ionospheric conductance and subcorotating auroral features within the ME was hypothesized by Rutala et al. (2022) as an explanation of subcorotational behavior near dawn. The basic premise is that, if the ionospheric conductance is locally increased for a reason unrelated to MI-coupling currents, the MI-coupling currents will increase in magnitude due to the heightened conductance, accelerating magnetospheric plasma up to the corotation rate of the planet; as the magnetosphere generally compresses from dawn through noon, the linear velocity of the recently-accelerated magnetospheric plasma would exceed the local angular corotational velocity as the system rotates, thus reducing or reversing the field-aligned currents. In the ionosphere, this would appear as a bright auroral form associated with the increased currents which ends abruptly as the currents reverse, thus appearing fixed in local time. This picture meshes well with the noon ME discontinuity observed by Radioti et al. (2008), which is expected to be associated with reduced or reversed field-aligned currents. The secondary peak in Σ_P^* near noon may be associated with the subcorotational noon auroral spot (Palmaerts et al., 2014), as following noon the magnetosphere expands again, thus requiring increased field-aligned currents to bring plasma up to local corotational velocity.

This second peak in Σ_P^* near 12 MLT may instead be caused by increased field-aligned currents caused by shearing motions of magnetospheric plasma, as modeled by Chané et al. (2018). Generally, as an increase in the field-aligned currents will cause an increase in the effective Pedersen conductance, we cannot distinguish between cause and effect with this data set: high currents could cause increased conductance, or heightened conductance may drive increased currents. It is of note that the conductance distributions found in Figure 8 are more similar to the modeled conductance distribution in LT found by Tao et al. (2010) than to the distributions in solar CML found by Gérard et al. (2020, 2021). In the latter case, the differences may in part be explained by the difference in observational integration time. Images from HST span non-overlapping 30–100 s exposures while spectral images from *Juno* were integrated over 20–50 min (Gérard et al., 2020, 2021), which would introduce more smoothing into the *Juno* UVS based maps than is present in this analysis. The similarity in form between the Σ_P^* distributions found here and those of Tao et al. (2010) may indicate a relationship between heightened dawn

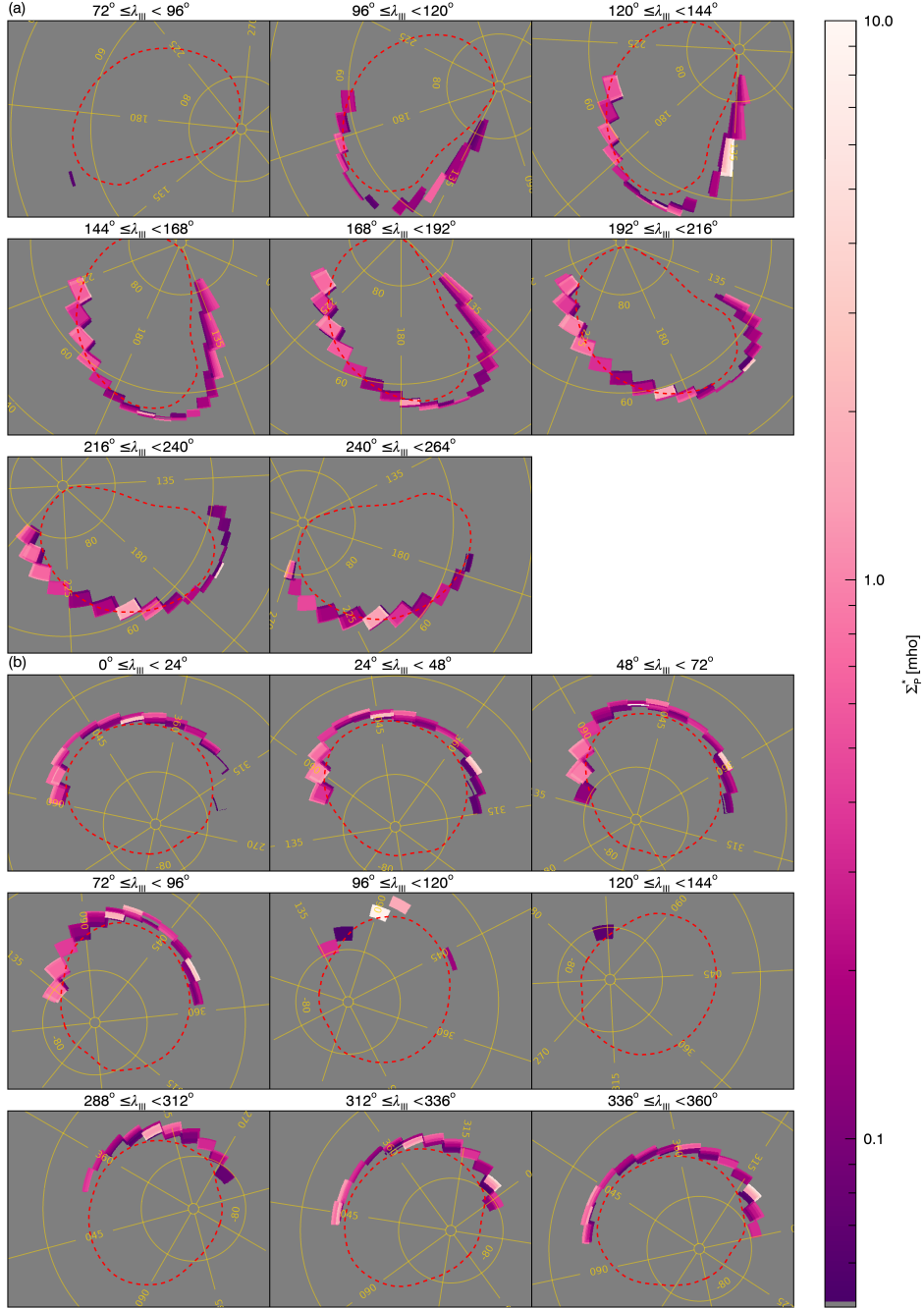


Figure 9. Polar, orthographic views of Jupiter’s north auroral region, with the derived Σ_P^* distributions shown mapped onto the planet by mapping MLT and ρ_e onto λ_{III} and ϕ . Each frame corresponds to one solar CML bin with the mean solar CML, and hence noon local time, located at the bottom of the image. The SMO is shown by a red-dashed line, and λ_{III} and ϕ graticules are shown in yellow. Values of Σ_P^* have been log-scaled and correspond to the colorbar to the right. The increased conductance near dawn, toward the left side of each frame, can be seen, as can the increased conductance at lower latitudes (mapping to smaller ρ_e).

462 sector conductance and incident solar extreme ultraviolet (EUV) photons, which increase
 463 the Pedersen conductance by ionizing the ionosphere.

464 5 Conclusions

465 We have outlined a novel method for deriving values of the effective Pedersen con-
 466 ductance Σ_P^* of Jupiter’s ME auroral ionosphere by combining remote observations of
 467 the Jovian ME and in-situ observations of the angular velocity, or corotation rate, of mid-
 468 dle magnetospheric plasma. This method has been developed from the theoretical un-
 469 derstanding of MI coupling at Jupiter, which links the field-aligned currents entering the
 470 ionosphere, estimated from the auroral brightness measured with HST, to the motion
 471 of middle magnetospheric plasma, calculated by moment analysis of *Galileo* PLS mea-
 472 surements. Equivalent regions of the auroral ionosphere and equatorial magnetosphere
 473 are found using magnetic flux equivalence mapping. The non-overlapping 288 HST ob-
 474 servations and 6751 *Galileo* measurements used in this analysis are taken to be repre-
 475 sentative of the time-averaged Jupiter system.

476 From the HST observations, we find field-aligned currents entering the ionosphere
 477 of $I_{\parallel} = 9.54_{-6.35}^{+11.5}$ MA rad⁻¹ and $I_{\parallel} = 10.6_{-6.11}^{+11.1}$ MA rad⁻¹, corresponding to the north-
 478 ern and southern ME, respectively, in agreement with recent *Juno*-based measurements
 479 (Kotsiaros et al., 2019; Nichols & Cowley, 2022) and theoretical estimates (Hill, 2001;
 480 Cowley & Bunce, 2001). Combining these values with the parameter I_{\parallel}/Σ_P^* derived from
 481 in-situ *Galileo* PLS measurements, we find the effective Pedersen conductance Σ_P^* , re-
 482 duced from the true Pedersen conductance by a factor of $1 - k \approx 0.5$. Σ_P^* ranges be-
 483 tween $0.03 < \Sigma_P^* < 1.79$ mho in the north and $0.02 < \Sigma_P^* < 2.26$ mho in the south, with
 484 typical values of $\Sigma_P^* = 0.14_{-0.08}^{+0.31}$ mho and $\Sigma_P^* = 0.14_{-0.09}^{+0.34}$ mho in the northern and
 485 southern ME, respectively. These typical values are consistent with theoretical and mod-
 486 eled values (Millward et al., 2002, 2005; Gérard et al., 2020, 2021), but the distributions
 487 of Σ_P^* we find reveal that it varies primarily in MLT, rather than solar CML. This anal-
 488 ysis indicates that the field-aligned currents derived from MI coupling theory, which have
 489 historically been used to explain Jupiter’s ME, adequately describe the relationship be-
 490 tween ME auroral brightness and the motion of middle magnetospheric plasma. Further,
 491 the heightened effective Pedersen conductance near MLTs of 07–08 and 12–13 MLT
 492 we find are approximately co-located with auroral features in the ME with subcorota-
 493 tional motions (Rutala et al., 2022; Radioti et al., 2008; Palmaerts et al., 2014). The re-
 494 sults we present are compatible with the theory that solar EUV ionization of the auro-
 495 ral ionosphere is key to controlling the motions of subcorotational auroral features in the
 496 dawn sector. We cannot, however, distinguish between this case and the case of otherwise-
 497 increased dawn currents causing locally elevated conductances. Breaking the observa-
 498 tional degeneracy between these cases should be done with comparisons of the distribu-
 499 tions found here to models of the field-aligned currents flowing in the MI coupling sys-
 500 tem under varying ionospheric conductance conditions.

Open Research

All Hubble Space Telescope observations used in this analysis are available at the Mikulski Archive for Space Telescopes hosted by the Space Telescope Science Institute, and have been collected into a single dataset for ease of access (Rutala, 2022). All *Galileo* PLS real-time-science data are available through the Planetary Plasma Interaction (PPI) node of the Planetary Data System (PDS) (Frank et al., 2023). This research made use of the ionosphere-magnetosphere mapping code of Vogt et al. (2011) and the internal magnetic field model of Connerney et al. (2022) as made available by Wilson et al. (2023) to allow comparison between in-situ and remote measurements.

Acknowledgments

This work is based on observations with the NASA/ESA Hubble Space Telescope, obtained from the Mikulski Archive for Space Telescopes (MAST) at the Space Telescope Science Institute (STScI). STScI is operated by the Association of Universities for Research in Astronomy, Inc, under NASA contract NAS5-26555. The work presented here was primarily supported by Space Telescope Science Institute (STScI) awards HST-GO-16675.002-A and HST-GO-16989.002-A to Boston University. Additionally, M. F. Vogt was supported in part by NASA grant 80NSSC17K0777. Finally, the authors would like to thank P. Withers for valuable input on the final form of this manuscript.

References

- Acton, C., Bachman, N., Semenov, B., & Wright, E. (2018, January). A look towards the future in the handling of space science mission geometry. *Planetary and Space Science*, *150*, 9–12. doi: 10.1016/j.pss.2017.02.013
- Allegrini, F., Kurth, W. S., Elliott, S. S., Saur, J., Livadiotis, G., Nicolaou, G., . . . Wilson, R. J. (2021). Electron Partial Density and Temperature Over Jupiter’s Main Auroral Emission Using Juno Observations. *Journal of Geophysical Research: Space Physics*, *126*(9), e2021JA029426. doi: 10.1029/2021JA029426
- Avila, R. J., Bohlin, R., Hathi, N., Lockwood, S., Lim, P. L., & De La Peña, M. (2019, October). *SBC Absolute Flux Calibration* (Tech. Rep.). Space Telescope Science Institute.
- Bagenal, F., Wilson, R. J., Siler, S., Paterson, W. R., & Kurth, W. S. (2016, May). Survey of Galileo plasma observations in Jupiter’s plasma sheet. *Journal of Geophysical Research: Planets*, *121*(5), 871–894. doi: 10.1002/2016JE005009
- Bonfond, B., Gladstone, G. R., Grodent, D., Greathouse, T. K., Versteeg, M. H., Hue, V., . . . Kurth, W. S. (2017, May). Morphology of the UV aurorae Jupiter during Juno’s first perijove observations. *Geophysical Research Letters*, *44*(10), 4463–4471. doi: 10.1002/2017GL073114
- Bonfond, B., Gustin, J., Gérard, J. C., Grodent, D., Radioti, A., Palmaerts, B., . . . Tao, C. (2015, October). The far-ultraviolet main auroral emission at Jupiter - Part 1: Dawn-dusk brightness asymmetries. *Annales Geophysicae*, *33*(10), 1203–1209. doi: 10.5194/angeo-33-1203-2015
- Bonfond, B., Yao, Z., & Grodent, D. (2020, November). Six Pieces of Evidence Against the Corotation Enforcement Theory to Explain the Main Aurora at Jupiter. *Journal of Geophysical Research: Space Physics*, *125*(11), e28152. doi: 10.1029/2020JA028152
- Bonfond, B., Yao, Z. H., Gladstone, G. R., Grodent, D., Gérard, J. C., Matar, J., . . . Bolton, S. J. (2021, March). Are Dawn Storms Jupiter’s Auroral Substorms? *AGU Advances*, *2*(1), e00275. doi: 10.1029/2020AV000275
- Caldwell, J., Turgeon, B., & Hua, X. M. (1992, September). Hubble space telescope imaging of the north polar aurora on jupiter. *Science*, *257*(5076), 1512–1515. doi: 10.1126/science.257.5076.1512

- 551 Chané, E., Palmaerts, B., & Radioti, A. (2018, September). Periodic shearing motions in the Jovian magnetosphere causing a localized peak in the main auroral
552 emission close to noon. *Planetary and Space Science*, *158*, 110–117. doi:
553 10.1016/j.pss.2018.04.023
- 554
555 Clarke, J. T., Grodent, D., Cowley, S. W. H., Bunce, E. J., Zarka, P., Connerney,
556 J. E. P., & Satoh, T. (2004). Jupiter’s aurora. In F. Bagenal, T. E. Dowling,
557 & W. B. McKinnon (Eds.), *Jupiter. The Planet, Satellites and Magnetosphere*
558 (Vol. 1, pp. 639–670).
- 559 Clarke, J. T., Nichols, J., Gérard, J.-C., Grodent, D., Hansen, K. C., Kurth, W., ...
560 Cecconi, B. (2009). Response of Jupiter’s and Saturn’s auroral activity to the
561 solar wind. *Journal of Geophysical Research: Space Physics*, *114*(A5). doi:
562 10.1029/2008JA013694
- 563 Connerney, J. E. P., Kotsiaros, S., Oliverson, R. J., Espley, J. R., Joergensen, J. L.,
564 Joergensen, P. S., ... Levin, S. M. (2018). A New Model of Jupiter’s Magnetic
565 Field From Juno’s First Nine Orbits. *Geophysical Research Letters*, *45*(6),
566 2590–2596. doi: 10.1002/2018GL077312
- 567 Connerney, J. E. P., Timmins, S., Oliverson, R. J., Espley, J. R., Joergensen, J. L.,
568 Kotsiaros, S., ... Levin, S. M. (2022, February). A New Model of Jupiter’s
569 Magnetic Field at the Completion of Juno’s Prime Mission. *Journal of Geo-*
570 *physical Research: Planets*, *127*(2), e07055. doi: 10.1029/2021JE007055
- 571 Cowley, S. W. H., & Bunce, E. J. (2001). Origin of the main auroral oval in
572 Jupiter’s coupled magnetosphere–ionosphere system. *Planetary and Space*
573 *Science*, *49*(10), 1067–1088. doi: 10.1016/S0032-0633(00)00167-7
- 574 Curran, P. A. (2014, November). Monte Carlo error analyses of Spearman’s rank
575 test. *arXiv e-prints*, arXiv:1411.3816.
- 576 Frank, L., Paterson, W., & Ackerson, K. (2023). *Galileo plasma science instru-*
577 *ment jupiter rts moments derived bundle* [dataset]. NASA Planetary Data Sys-
578 tem. Retrieved from [https://pds-ppi.igpp.ucla.edu/search/view/?id=](https://pds-ppi.igpp.ucla.edu/search/view/?id=pds://PPI/galileo-pls-jup-derived)
579 pds://PPI/galileo-pls-jup-derived doi: doi.org/10.17189/jbaw-bm37
- 580 Gérard, J.-C., Dols, V., Prangé, R., & Paresce, F. (1994). The morphology of
581 the north Jovian ultraviolet aurora observed with the Hubble Space Tele-
582 scope. *Planetary and Space Science*, *42*(11), 905–917. doi: 10.1016/
583 0032-0633(94)90051-5
- 584 Gérard, J.-C., Gkouvelis, L., Bonfond, B., Grodent, D., Gladstone, G. R., Hue, V.,
585 ... Blanc, M. (2020). Spatial Distribution of the Pedersen Conductance in the
586 Jovian Aurora From Juno-UVS Spectral Images. *Journal of Geophysical Re-*
587 *search: Space Physics*, *125*(8), e2020JA028142. doi: 10.1029/2020JA028142
- 588 Gérard, J.-C., Gkouvelis, L., Bonfond, B., Grodent, D., Gladstone, G. R., Hue, V.,
589 ... Giles, R. S. (2021). Variability and Hemispheric Symmetry of the Pedersen
590 Conductance in the Jovian Aurora. *Journal of Geophysical Research: Space*
591 *Physics*, *126*(4), e2020JA028949. doi: 10.1029/2020JA028949
- 592 Gérard, J. C., Grodent, D., Prange, R., Waite, J. H., Gladstone, G. R., Dols, V., ...
593 Franke, K. A. (1994, December). A Remarkable Auroral Event on Jupiter Ob-
594 served in the Ultraviolet with the Hubble Space Telescope. *Science*, *266*(5191),
595 1675–1678. doi: 10.1126/science.266.5191.1675
- 596 Gérard, J.-C., Grodent, D., Radioti, A., Bonfond, B., & Clarke, J. T. (2013). Hub-
597 ble observations of Jupiter’s north–south conjugate ultraviolet aurora. *Icarus*,
598 *226*(2), 1559–1567. doi: 10.1016/j.icarus.2013.08.017
- 599 Gérard, J. C., Mura, A., Bonfond, B., Gladstone, G. R., Adriani, A., Hue, V., ...
600 Levin, S. M. (2018, September). Concurrent ultraviolet and infrared obser-
601 vations of the north Jovian aurora during Juno’s first perijove. *Icarus*, *312*,
602 145–156. doi: 10.1016/j.icarus.2018.04.020
- 603 Greathouse, T., Gladstone, R., Versteeg, M., Hue, V., Kammer, J., Giles, R., ...
604 Vogt, M. F. (2021, December). Local Time Dependence of Jupiter’s Polar
605 Auroral Emissions Observed by Juno UVS. *Journal of Geophysical Research:*

- 606 *Planets*, 126(12), e06954. doi: 10.1029/2021JE006954
- 607 Grodent, D., Bonfond, B., Gérard, J.-C., Radioti, A., Gustin, J., Clarke, J. T.,
608 ... Connerney, J. E. P. (2008, September). Auroral evidence of a localized
609 magnetic anomaly in Jupiter’s northern hemisphere. *Journal of Geophysical*
610 *Research: Space Physics*, 113(A9), A09201. doi: 10.1029/2008JA013185
- 611 Grodent, D., Clarke, J. T., Kim, J., Waite, J. H., & Cowley, S. W. H. (2003,
612 November). Jupiter’s main auroral oval observed with HST-STIS. *Jour-*
613 *nal of Geophysical Research: Space Physics*, 108(A11), 1389. doi: 10.1029/
614 2003JA009921
- 615 Grodent, D., Gérard, J.-C., Cowley, S. W. H., Bunce, E. J., & Clarke, J. T. (2005).
616 Variable morphology of Saturn’s southern ultraviolet aurora. *Journal of Geo-*
617 *physical Research: Space Physics*, 110(A7). doi: 10.1029/2004JA010983
- 618 Gustin, J., Bonfond, B., Grodent, D., & Gérard, J.-C. (2012). Conversion from HST
619 ACS and STIS auroral counts into brightness, precipitated power, and radiated
620 power for H₂ giant planets. *Journal of Geophysical Research: Space Physics*,
621 117(A7). doi: 10.1029/2012JA017607
- 622 Hill, T. W. (1979, November). Inertial limit on corotation. *Journal of Geo-*
623 *physical Research: Space Physics*, 84(A11), 6554–6558. doi: 10.1029/
624 JA084iA11p06554
- 625 Hill, T. W. (2001). The Jovian auroral oval. *Journal of Geophysical Research: Space*
626 *Physics*, 106(A5), 8101–8107. doi: 10.1029/2000JA000302
- 627 Huang, T. S., & Hill, T. W. (1989, April). Corotation lag of the Jovian atmosphere,
628 ionosphere, and magnetosphere. *Journal of Geophysical Research: Space*
629 *Physics*, 94(A4), 3761–3765. doi: 10.1029/JA094iA04p03761
- 630 Huscher, E., Bagenal, F., Wilson, R. J., Allegrini, F., Ebert, R. W., Valek, P. W.,
631 ... Levin, S. M. (2021). Survey of Juno Observations in Jupiter’s Plasma
632 Disk: Density. *Journal of Geophysical Research: Space Physics*, 126(8),
633 e2021JA029446. doi: 10.1029/2021JA029446
- 634 Khurana, K. K., & Schwarzl, H. K. (2005, July). Global structure of Jupiter’s mag-
635 netospheric current sheet. *Journal of Geophysical Research: Space Physics*,
636 110(A7), A07227. doi: 10.1029/2004JA010757
- 637 Kita, H., Kimura, T., Tao, C., Tsuchiya, F., Murakami, G., Yamazaki, A., ... Fuji-
638 moto, M. (2019, December). Jovian UV Aurora’s Response to the Solar Wind:
639 Hisaki EXCEED and Juno Observations. *Journal of Geophysical Research:*
640 *Space Physics*, 124(12), 10,209–10,218. doi: 10.1029/2019JA026997
- 641 Kotsiaros, S., Connerney, J. E. P., Clark, G., Allegrini, F., Gladstone, G. R., Kurth,
642 W. S., ... Levin, S. M. (2019, July). Birkeland currents in Jupiter’s magneto-
643 sphere observed by the polar-orbiting Juno spacecraft. *Nature Astronomy*, 3,
644 904–909. doi: 10.1038/s41550-019-0819-7
- 645 Krupp, N., Lagg, A., Livi, S., Wilken, B., Woch, J., Roelof, E. C., & Williams, D. J.
646 (2001, November). Global flows of energetic ions in Jupiter’s equatorial plane:
647 First-order approximation. *Journal of Geophysical Research: Space Physics*,
648 106(A11), 26017–26032. doi: 10.1029/2000JA900138
- 649 Mauk, B. H., Clark, G., Gladstone, G. R., Kotsiaros, S., Adriani, A., Allegrini,
650 F., ... Rymer, A. M. (2020, March). Energetic Particles and Acceleration
651 Regions Over Jupiter’s Polar Cap and Main Aurora: A Broad Overview.
652 *Journal of Geophysical Research: Space Physics*, 125(3), e27699. doi:
653 10.1029/2019JA027699
- 654 Mauk, B. H., Haggerty, D. K., Paranicas, C., Clark, G., Kollmann, P., Rymer,
655 A. M., ... Valek, P. (2017, September). Discrete and broadband electron
656 acceleration in Jupiter’s powerful aurora. *Nature*, 549(7670), 66–69. doi:
657 10.1038/nature23648
- 658 Mauk, B. H., Haggerty, D. K., Paranicas, C., Clark, G., Kollmann, P., Rymer,
659 A. M., ... Valek, P. (2018, February). Diverse Electron and Ion Acceleration
660 Characteristics Observed Over Jupiter’s Main Aurora. *Geophysical Research*

- 661 *Letters*, 45(3), 1277–1285. doi: 10.1002/2017GL076901
- 662 Millward, G., Miller, S., Stallard, T., Achilleos, N., & Aylward, A. D. (2005, Jan-
663 uary). On the dynamics of the jovian ionosphere and thermosphere.. IV. Ion-
664 neutral coupling. *Icarus*, 173(1), 200–211. doi: 10.1016/j.icarus.2004.07.027
- 665 Millward, G., Miller, S., Stallard, T., Aylward, A. D., & Achilleos, N. (2002). On
666 the Dynamics of the Jovian Ionosphere and Thermosphere: III. The Modelling
667 of Auroral Conductivity. *Icarus*, 160(1), 95–107. doi: 10.1006/icar.2002.6951
- 668 Nichols, J. D., Allegrini, F., Bagenal, F., Bunce, E. J., Cowley, S. W. H., Ebert,
669 R. W., ... Yao, Z. (2020, August). An Enhancement of Jupiter’s Main Auro-
670 ral Emission and Magnetospheric Currents. *Journal of Geophysical Research:*
671 *Space Physics*, 125(8), e27904. doi: 10.1029/2020JA027904
- 672 Nichols, J. D., Badman, S. V., Bagenal, F., Bolton, S. J., Bonfond, B., Bunce,
673 E. J., ... Yoshikawa, I. (2017, August). Response of Jupiter’s auroras to
674 conditions in the interplanetary medium as measured by the Hubble Space
675 Telescope and Juno. *Geophysical Research Letters*, 44(15), 7643–7652. doi:
676 10.1002/2017GL073029
- 677 Nichols, J. D., Clarke, J. T., Gérard, J. C., Grodent, D., & Hansen, K. C. (2009,
678 June). Variation of different components of Jupiter’s auroral emission.
679 *Journal of Geophysical Research: Space Physics*, 114(A6), A06210. doi:
680 10.1029/2009JA014051
- 681 Nichols, J. D., & Cowley, S. (2004, May). Magnetosphere-ionosphere coupling
682 currents in Jupiter’s middle magnetosphere: Effect of precipitation-induced
683 enhancement of the ionospheric Pedersen conductivity. *Annales Geophysicae*,
684 22(5), 1799–1827. doi: 10.5194/angeo-22-1799-2004
- 685 Nichols, J. D., & Cowley, S. W. H. (2003, July). Magnetosphere-ionosphere coupling
686 currents in Jupiter’s middle magnetosphere: Dependence on the effective iono-
687 spheric Pedersen conductivity and iogenic plasma mass outflow rate. *Annales*
688 *Geophysicae*, 21(7), 1419–1441. doi: 10.5194/angeo-21-1419-2003
- 689 Nichols, J. D., & Cowley, S. W. H. (2005, March). Magnetosphere-ionosphere
690 coupling currents in Jupiter’s middle magnetosphere: Effect of magnetosphere-
691 ionosphere decoupling by field-aligned auroral voltages. *Annales Geophysicae*,
692 23(3), 799–808. doi: 10.5194/angeo-23-799-2005
- 693 Nichols, J. D., & Cowley, S. W. H. (2022). Relation of Jupiter’s Dawnside Main
694 Emission Intensity to Magnetospheric Currents During the Juno Mission.
695 *Journal of Geophysical Research: Space Physics*, 127(1), e2021JA030040. doi:
696 10.1029/2021JA030040
- 697 Palmaerts, B., Radioti, A., Grodent, D., Chané, E., & Bonfond, B. (2014). Tran-
698 sient small-scale structure in the main auroral emission at Jupiter. *Jour-*
699 *nal of Geophysical Research: Space Physics*, 119(12), 9931–9938. doi:
700 10.1002/2014JA020688
- 701 Radioti, A., Gérard, J.-C., Grodent, D., Bonfond, B., Krupp, N., & Woch, J. (2008).
702 Discontinuity in Jupiter’s main auroral oval. *Journal of Geophysical Research:*
703 *Space Physics*, 113(A1). doi: 10.1029/2007JA012610
- 704 Ray, L. C., Achilleos, N. A., Vogt, M. F., & Yates, J. N. (2014). Local time
705 variations in Jupiter’s magnetosphere-ionosphere coupling system. *Jour-*
706 *nal of Geophysical Research: Space Physics*, 119(6), 4740–4751. doi:
707 10.1002/2014JA019941
- 708 Ray, L. C., Ergun, R. E., Delamere, P. A., & Bagenal, F. (2010). Magnetosphere-
709 ionosphere coupling at Jupiter: Effect of field-aligned potentials on angu-
710 lar momentum transport. *Journal of Geophysical Research: Space Physics*,
711 115(A9). doi: 10.1029/2010JA015423
- 712 Rutala, M. J. (2022). *Data for rutala et al. 2022* [dataset]. MAST. Retrieved from
713 [https://archive.stsci.edu/doi/resolve/resolve.html?doi=10.17909/](https://archive.stsci.edu/doi/resolve/resolve.html?doi=10.17909/ekt0-mf55)
714 [ekt0-mf55](https://archive.stsci.edu/doi/resolve/resolve.html?doi=10.17909/ekt0-mf55) doi:doi:10.17909/ekt0-mf55
- 715 Rutala, M. J., Clarke, J. T., Mullins, J. D., & Nichols, J. D. (2022, June). Illuminat-

- 716 ing the Motions of Jupiter’s Auroral Dawn Storms. *Journal of Geophysical Re-*
717 *search: Space Physics*, 127(6), e30448. doi: 10.1029/2022JA030448
- 718 Smith, C. G. A., & Aylward, A. D. (2009, January). Coupled rotational dynamics of
719 Jupiter’s thermosphere and magnetosphere. *Annales Geophysicae*, 27(1), 199–
720 230. doi: 10.5194/angeo-27-199-2009
- 721 Southwood, D. J., & Kivelson, M. G. (2001). A new perspective concerning the in-
722 fluence of the solar wind on the Jovian magnetosphere. *Journal of Geophysical*
723 *Research: Space Physics*, 106(A4), 6123–6130. doi: 10.1029/2000JA000236
- 724 Tao, C., Fujiwara, H., & Kasaba, Y. (2009, August). Neutral wind control of the
725 Jovian magnetosphere-ionosphere current system. *Journal of Geophysical Re-*
726 *search: Space Physics*, 114(A8), A08307. doi: 10.1029/2008JA013966
- 727 Tao, C., Fujiwara, H., & Kasaba, Y. (2010). Jovian magnetosphere–ionosphere
728 current system characterized by diurnal variation of ionospheric conductance.
729 *Planetary and Space Science*, 58(3), 351–364. doi: 10.1016/j.pss.2009.10.005
- 730 Vogt, M. F., Kivelson, M. G., Khurana, K. K., Walker, R. J., Bonfond, B., Grodent,
731 D., & Radioti, A. (2011). Improved mapping of Jupiter’s auroral features
732 to magnetospheric sources. *Journal of Geophysical Research: Space Physics*,
733 116(A3). doi: 10.1029/2010JA016148
- 734 Walker, R. J., & Ogino, T. (2003, April). A simulation study of currents in the Jo-
735 vian magnetosphere. *Planetary and Space Science*, 51(4-5), 295–307. doi: 10
736 .1016/S0032-0633(03)00018-7
- 737 Wilson, R. J., Vogt, M. F., Provan, G., Kamran, A., James, M. K., Brennan, M.,
738 & Cowley, S. W. H. (2023, February). Internal and external jovian mag-
739 netic fields: Community code to serve the magnetospheres of the outer planets
740 community. , 219(15), 15. doi: 10.1007/s11214-023-00961-3